ELSEVIER

Marine and Petroleum Geology 22 (2005) 551–568

Marine and Petroleum Geology

www.elsevier.com/locate/marpetgeo

Measurement of marine hydrocarbon seep flow through fractured rock and unconsolidated sediment

Ira Leifer[a,*], Jim Boles[b]

[a]Marine Sciences Institute, University of California, Santa Barbara, CA 93106, USA
[b]Department of Geological Sciences, University of California, Santa Barbara, CA 93106, USA

Received 28 October 2003; accepted 1 October 2004

Abstract

Three turbine seep-tents measured gas flux variations including an ejection at one tent. Several conceptual models of hydrocarbon migration were developed from the relationship between fluxes at the tents. (1) A resistor—capacitor network to model oil and gas flux in the seep system including an oil regulator model. (2) A fracture oil-deposition model where oil deposited on fracture walls progressively clogs and then blocks fractures. Also measured were bubble size distributions for minor and major vents that were narrow, and broad, respectively, and varied with time due to oil flux. Very oily bubbles with different trajectories were observed.

Keywords: Marine hydrocarbon seepage; Petroleum migration; Bubble measurement

1. Introduction

Oil and gas seepage into the marine environment and subsurface migration pathways are of interest and concern to a wide spectrum of professionals. Due to the difficulty (both technical and regulatory) of planned petroleum release experiments, perennial marine hydrocarbon seeps provide an *ideal natural laboratory* for the study of hydrocarbon migration into the environment. The escaping bubble streams provide an easily identifiable locator of active seepage, both visually and acoustically (sonar). Moreover, in cases where the sediment overburden is thin, the seabed provides a roughly horizontal, planar transect through a fracture network, thereby allowing non-destructive study of multiphase migrational processes. And since seeps respond to external forcing—e.g. tidal (Boles et al., 2001), swell (Leifer and Boles, 2004), and potentially others, such as earthquakes (Leifer et al., 2003a)—the response to the forcing perturbations serves as a probe of subsurface processes. Thus, our approach for several years has been to focus on intensive characterization of a highly active seep area located in the Coal Oil Point (COP) seep field, California, documenting seep behaviour at various time scales.

During these studies, the University of California, Santa Barbara (UCSB) has developed the capability to measure simultaneously temporal seepage variations at multiple locations. In conjunction with other observations, this has allowed the development of a conceptual model describing some aspects of the near seabed migration of oil, gas, and tar through a subsurface fracture network. The data show that seepage at different vents is related so that an event through one fracture affects other vents. The purpose of this paper is to present the methodology and results from this work as well as a conceptual model of oil–gas migration for the shallow subsurface in the COP seep field. Two conceptual models were developed and are presented in this paper. The first model proposes simulating oil–gas migration as a network of connected resistors and capacitors and provides a useful mechanism for understanding how flux at one vent is related to flux at another vent. The second model proposes a punctuated tar migration mechanism that can explain the formation of large transient emission events.

Our purpose is to show that hydrocarbon flux is spatially and temporally variable in a multiphase system. Marine hydrocarbon seeps are an ideal natural laboratory to study these interrelated processes and the COP seep field has been

* Corresponding author. Tel.: +1 805 893 4941; fax: +1 805 893 4731.
E-mail address: ira.leifer@bubbleology.com (I. Leifer).

0264-8172/$ - see front matter © 2005 Elsevier Ltd. All rights reserved.
doi:10.1016/j.marpetgeo.2004.10.026

Nomenclature

R	Resistance
C	Capacitance
V_D	Driving voltage potential
V_E	Emission voltage
i	Current
r	Equivalent spherical radius
r_P	Peak radius in a bubble distribution
t	Time
s	Surfactant (presence or absence)
p	Oil-to-gas ratio
Q	Flux through a seep tent
P	Rotation rate of the turbine seep-tent turbine
$V_x(t)$	Horizontal bubble velocity (same as horizontal water velocity) (cm s^{-1})
$V_z(r,t)$	Vertical bubble velocity (cm s^{-1})
V_B	Stagnant water bubble buoyancy velocity(cm s^{-1})
V_{up}	Upwelling fluid velocity (cm s^{-1})
$\Psi(r,t)$	Bubble-size layer-population distribution (no. μm^{-1} m^{-1})
$\Phi(r,t)$	Bubble-size emission-population distribution (no. μm^{-1} s^{-1})

studied more extensively than any other seep field in the world. Although specific details of interconnectivity may vary for hydrocarbon seeps in other parts of the world (for example due to substrate, absence of tar and/or oil, etc.), the mechanisms and many aspects of the seepage should be applicable to other hydrocarbon seeps. Moreover, the basic mechanisms underlying the multiphase migration of oil, gas, tar, and water, and studied in the shallow subsurface at COP, can be applied to migration through fractures at much greater depths where the flow is still multiphase. Finally, these results are the first to show the importance of quantifying both the temporal and spatial variability in seepage for interpretation and extrapolation of observations.

1.1. Background

Hydrocarbon seepage provides an important path for methane to leak from the lithosphere to the hydrosphere and atmosphere. Given methane's importance as a greenhouse gas, quantifying methane sources and sinks is important to understanding its budget. Current global flux estimates suggest seepage contributes 35–45 Tg yr^{-1} (Etiope and Klusman, 2002) from both terrestrial and marine sources, i.e. approximately 7% of the global atmospheric methane budget of 540 Tg yr^{-1} (Prather et al., 1995). Thus, seep emissions are comparable to other important sources, such as termites (Khalil and Rasmussen, 1995). Of the seep flux, the marine contribution was estimated conservatively at 20 Tg yr^{-1} (Kvenvolden et al., 2001) and arises primarily from hydrate and thermogenic sources. However, significant uncertainties remain in estimates of the fraction of emitted methane that reaches the atmosphere, particularly since few quantitative measurements of seepage flux exist.

Furthermore, most existing quantitative measurements do not address temporal—much less spatial—variations in these highly dynamic systems, even though seeps vary on time scales from the tidal (Tryon et al., 1999; Boles et al., 2001) to decadal (Fischer and Stevenson, 1973; Boles et al., 2001). These include transient releases of large magnitude associated with significant seabed morphological changes (Leifer et al., 2004). Thus, current budgets may be significant underestimates of the contribution of marine and terrestrial methane as they do not include the effect of large transient releases. Furthermore, large transient releases affect the ambient environment (upwelling flow and plume fluid saturation), potentially allowing a significantly greater percentage of the escaping seabed methane to reach the atmosphere from greater depths (Leifer and Patro, 2002; Clark et al., 2003). The importance of transient emissions may have even greater significance if warming ocean temperatures lead to widespread hydrate destabilization as suggested by the Clathrate Gun Hypothesis of Kennett et al. (2003).

1.2. Seep size scales

In the COP seep field, seep areas are spatially distinct and, on a kilometre scale, are controlled by the underlying fault structure (Fischer, 1978); as a result, seeps are located primarily along several distinct trends. As is typical for many natural—including geologic—systems (Mandelbrot, 2002), hydrocarbon seepage exhibits spatial structures on many different scales, from the kilometre to the centimetre. Since the interrelationship between scales and controlling processes is critical to this manuscript, we propose a terminology of hydrocarbon seepage structures, illustrated in Fig. 1. This proposed terminology describes seabed seepage where the seabed is sufficiently cohesive that vents are fixed over time scales long compared to the bubble emission rate or pulse emission rate.

At the largest scale is the *seep field*, which is isolated from other seep fields by large distances (large is defined as greater than 20 times the size scale of the structure, in this case, the seep field). Within the seep field are active *seep areas* that are surrounded by areas without seepage. Often, these seep areas are controlled by the underlying geological structures (faults, fractures, salt diapirs, caprocks, etc.) and may span several to tens (or even hundreds) of metres. A seep area may contain a *central seep zone* or *zones* that defined by distinct morphological features (mud volcanoes,

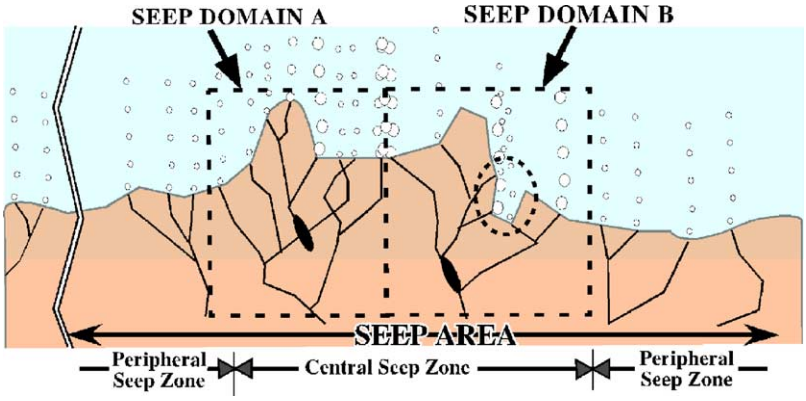

Fig. 1. Schematic illustrating seep size scale definitions. See text for more details.

mounds, brine pools, etc.) and may be surrounded by an active (though typically much less so, and thus the absence of significant features) *peripheral seep zone*. A seep area can contain multiple central seep zones or even none, but only one peripheral zone. At the smallest scale (neglecting microseepage) is the *seep vent*, from which bubbles emerge at a single point. Thus, even a small pit, whose dimensions are a few vent mouth diameters, can contain several vents (see circled area in Seep Domain B in Fig. 1). Finally, structures larger than seep vents can exist within the seep zones and are termed *seep domains*. By our definition, we define the extent of a seep zone as containing seep vents that exhibit close interconnectedness. Thus within the domain, flux variations at one vent strongly affect the flux at other vents. Also, some of the vents in a seep domain may be physically located in another seep domain; it is the connectivity that is important. Finally, in some cases a seep field may consist of a single seep area.

1.3. Seep field description

The COP seep field is one of the largest known areas of active marine seepage in the world and is located a few kilometres from the UCSB campus. A map of informally named seeps in the field and sonar mapped areas of seepage is shown in Fig. 2. Several studies have quantified the COP seep field seep area (e.g. Allen et al., 1970; Fischer and Stevenson, 1973) and emission fluxes in the Santa Barbara Channel (e.g. Hornafius et al., 1999; Quigley et al., 1999; Clark et al., 2000) based on sonar techniques, flux buoys, and direct gas capture. During the last seven years, the UCSB seep group has mapped the seeps in the area using sonar and quantified seepage flux from sonar and direct gas capture using a flux buoy (Washburn et al., 2001). Results indicate that $\sim 1.5\times10^5$ m^3 dy^{-1} (5×10^6 ft^3 dy^{-1}) of seep gas escapes from ~ 3 km^2 of sea floor to the atmosphere (Hornafius et al., 1999) with roughly an equal amount injected into the coastal ocean (Clark et al., 2000). Most seepage is located along linear trends above faults or fractured anticlines. The inner trend is at ~ 20 m water depth and includes the Farrar Seep, IV Super Seep, and Shane Seep. A second trend at ~ 40 m depth includes the Horseshoe and Coal Oil Point Seeps. The deepest trend is at ~ 70 m depth and includes the La Goleta and Seep Tent Seeps as well as Platform Holly. This trend corresponds to the intersection of the South Ellwood Fault with the ocean

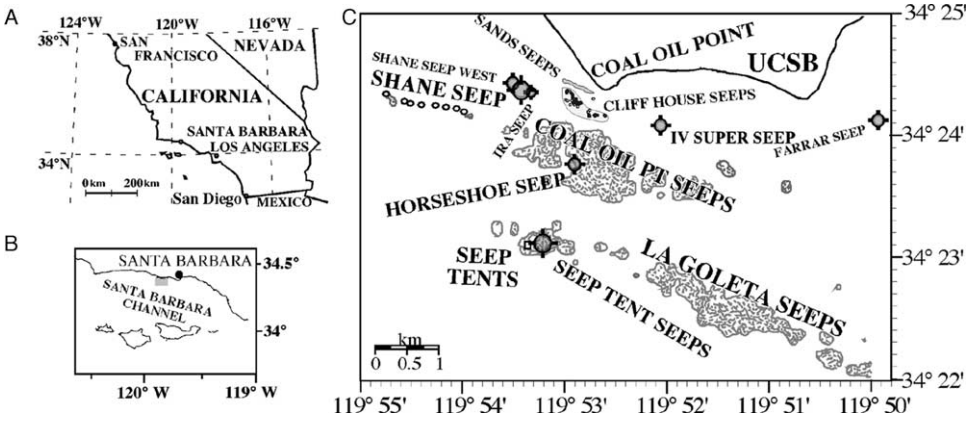

Fig. 2. Location of informally named seeps in the Coal Oil Point seep field, Santa Barbara Channel off the coast of Santa Barbara, California. Upper right panel shows the southwest US coast; upper left panel shows the Santa Barbara Channel with gray rectangle indicating the location of the study area, shown in lower panel. Gray areas in lower panel indicate regions of high bubble density from sonar returns (Hornafius et al., 1999). Inshore seeps (Shane Seep, IV Super Seep, and Farrar Seep) were too shallow for the survey.

floor (Fischer, 1978). Seepage continues to occur along the S. Ellwood Fault despite recharging of sub-hydrostatic reservoir pressure by seawater moving down the fault (Boles and Horner, 2003), indicating the flow is buoyancy driven along large fractures.

Seep structures are quasi-permanent, depending on the time scale. Thus, there is evidence that hydrocarbon seepage has been escaping from the basin margin for more than 100,000 years (Boles et al., 2004) in areas at least 5 km north of the COP seep field. In the present Santa Barbara Channel, seep areas are transient on a decadal time scale and the seep field's extent varies considerably. Fischer and Stevenson (1973) noted decadal time scale changes in the COP seep field with a significant decrease in seepage areas between 1946 and 1973 based on a comparison of sonar data and oil company seep maps.

One well-documented example of significant seep area variability is the appearance of the Seep Tent Seep (the largest seep area in the field) in 1978. Its most active seepage areas (central seep zones) were capped by two large (30 m by 30 m) seep tents that capture the gas from which a pipe transports it onshore. When deployed in 1982, the tents captured 16,800 m^3 dy^{-1}. Since then tent output has been monitored hourly. Analysis shows significant variations on hourly to decadal time scales (Boles et al., 2001). Variations on time scales from months to years also were documented for seep zones during a series of seabed surveys of a second highly active seep area, Shane Seep. Seep vents and seep domains were documented to 'persist' for similar time scales, although their persistence is partially controlled by seep zone changes, i.e. seep zone (e.g. a hydrocarbon volcano) relocation typically terminates vents and seep domains at the former location (Leifer et al., 2004).

1.4. Oily-seep bubbles

Seepage in the COP seep field primarily occurs as oil-coated bubbles. Although most details of the behaviour of oil-coated bubbles remain unquantified, the effects of an oil coating likely are great, both on hydrodynamics and gas exchange. Oil affects bubbles both directly and indirectly. Oil directly decreases the bubble's buoyancy. Oil also decreases the flow around the rising bubble in the boundary layer by damping capillary waves on the bubble interface (oil is surface active), thereby altering the bubble's hydrodynamics. Although observations demonstrate that oil strongly affects bubble behaviour (MacDonald et al., 2002; Leifer and MacDonald, 2003) given the absence of parameterizations of oily bubble behaviour, it is not possible to predict the fate of oily bubbles as they rise through the water column and are advected by oceanic currents.

Although most details of the behaviour of oily ocean bubbles remains unknown, oil clearly effects hydrodynamics (Leifer and MacDonald, 2003) and bubble buoyancy (by reducing it), leading to a decreased rise speed. Thus, by comparing the measured bubble rise velocity with the predicted rise-velocity of an oil-free bubble, an estimate of the quantity of oil on each bubble can be inferred. Then, from the time series of this inferred oil quantity, conclusions can be drawn regarding the time variability of the oil flux.

Since producing oily bubbles in the laboratory is highly challenging, marine seeps provide an ideal opportunity to test assumptions of oily-bubble parameterizations and to investigate the relationships between bubble size, emission flux, oil–gas ratio, and temporal variability. Observations in the Gulf of Mexico for bubbles escaping an exposed hydrate mound at 550-m depth showed an inverse relationship between bubble oiliness and bubble gas flux for different vents. Also, vent age was correlated with oiliness and gas flow (Leifer and MacDonald, 2003).

Rising bubble plumes create an upwelling flow that lifts deeper water towards shallower depths (Leifer et al., 2000a) thereby causing bubbles to rise faster than in the absence of such flows. The upwelling flow depends upon bubble size and the gas flux, as well as parameters that affect bubble hydrodynamics. One of these parameters is the state of the bubble surface, clean or dirty. By comparison with lab experiments, we conclude that the bubble vertical velocity data presented below is best explained if bubbles were dirty.

Hydrodynamically clean bubbles have mobile interfaces, rise faster, and exchange gas faster, while dirty bubbles, those with oil or surfactants, surface-active substances, on their interface, have immobile interfaces, rise slower, and exchange gas slower (Leifer and Patro, 2002). Bubbles may be in contaminated water (i.e. not distilled) and still behave as though they were hydrodynamically clean. The stagnant cap model (Sadhal and Johnson, 1983) describes the behaviour of a surfactant on a bubble, and describes how the flow around the rising bubble compresses the surfactant into the downstream hemisphere of the bubble's surface. This model predicts that a surfactant has minimal effect on bubble hydrodynamics unless the surfactant 'cap' extends past 45° from the bubble's downstream pole. Once the cap extends beyond 45°—for example on a dissolving bubble, or where contamination is increasing with time—the bubble rapidly transitions from clean to dirty behaviour. Thus, numerical simulations of bubble processes should use a parameterization for bubble gas exchange and rise velocity that shifts from dirty to clean at a transition radius (Leifer and Patro, 2002).

The stagnant cap model was confirmed experimentally for industrial surfactants (Duineveld, 1995) and showed that 'clean' versus 'dirty' behaviour depended on the amount of surfactant on the bubble and the bubble size. Patro et al. (2002) showed that in seawater, bubbles larger than about 700-μm radius behaved clean while smaller bubbles behaved dirty. For more contaminated water, such as from a saltwater marsh, the transition occurred at larger radius. Because oil is surface active, oil-contaminated bubbles should show similarities to surfactant-contaminated bubbles, assuming for most bubbles the oil contamination was not too great. Clearly, if bubble oil contamination was

sufficiently large, bubble buoyancy will be reduced, among other bubble properties.

2. Methodology

2.1. Turbine seep-tent

A turbine seep-tent was developed and three were deployed in the COP seep field to study hydrocarbon gas migration through a fracture network. The design, calibration, and some initial results are reported in detail in Leifer and Boles (2005). The tents (Fig. 3A) are an inexpensive design to maximize the number for deployment. In brief, the tents work by converting the upwelling flow into turbine rotations that are related to the gas flux. Bubbles are collected by an inverted funnel, 2-m diameter, and 1-m tall. To minimize the effect of the bubble size distribution on the upwelling flow (and hence the rotation rate for a given flow), bubbles pass through a breakup grid that converts the seep-bubble size-distribution to a monodisperse distribution before entering a chimney where the turbine is mounted. Four magnets mounted on the turbine shaft produce a signal in a Hall Effect sensor that is recorded by a multichannel data logger. Laboratory calibration by bubbling air from three distinctly different air stones (and thus size distributions) into a submerged tent showed very good correlation for,

$$Q = 104.42 \times P^{1.82} \quad (1)$$

where Q is flow (L s^{-1}) and P is rotation rate. Flow rates were measured with rotameter/flow controllers spanning 5 cm^3 s^{-1} to 23,600 cm^3 s^{-1} (FL3840C, FL31615A, FL-3804ST, HFL2709A, HFL6760A, HF2709A, and HF6760A, Omega Engineering, CT) and were corrected for the hydrostatic pressure at the turbine. The correlation was good for $0.015 < Q < 20$ L s^{-1} (i.e. three orders of magnitude of gas flux) with a correlation coefficient of 0.985. For lower flow ($Q < 0.015$), friction and inertia caused (1) to overestimate the spin rate for a given flow rate. The number of pulses per time interval (0.2 s) was recorded and thus Q was highly quantized. The data were subjected to both a running sum average followed by a block average to reduce the quantization. A conductivity temperature device (Model SB-39, Seabird, FL) recorded the seabed pressure and temperature with 3-s time resolution. Gas fluxes were corrected to standard temperature and pressure (STP) using the CTD data.

2.2. Bubble measurement system

A video bubble measurement system (BMS) was developed and deployed in the COP seep field to quantify the bubble size and time flux (Fig. 3B). To calculate the bubble flux, analysis of BMS data yields the vertical bubble velocity and thus also measures bubble and bubble-plume hydrodynamics. BMS systems and analysis approaches are reviewed in Leifer et al. (2003b). The BMS has several key components. Bubbles were backlit by two 300-Watt, wide dispersion, underwater lights shining on a translucent screen. Backlighting causes bubbles to appear as dark rings surrounded by central bright spots. This allows computer analysis, at least in principle. In contrast, side lighting produces half moons requiring manual outlining (Leifer and MacDonald, 2003). The measurement volume's far edge is maintained distant from the translucent screen by a clear screen with size scale markings (dots separated by 1 cm). This prevents bubbles from rising too close to the illumination screen where off-axis rays obscure the bubble's edges, decreasing contrast and biasing bubble radius, r, towards a potentially significant underestimate (Leifer et al., 2003c). One bubble blocker prevented bubbles from rising between the camera and measurement volume, while a second blocker prevented bubbles from rising behind the screen and casting shadows. Long focal length settings minimize parallax errors within the measurement volume. The underwater video camera (SuperCam 6500, DeepSea Power and Light, San Diego, CA) allowed complete remote control, including shutter speed, which must be set sufficiently fast to prevent blurring.

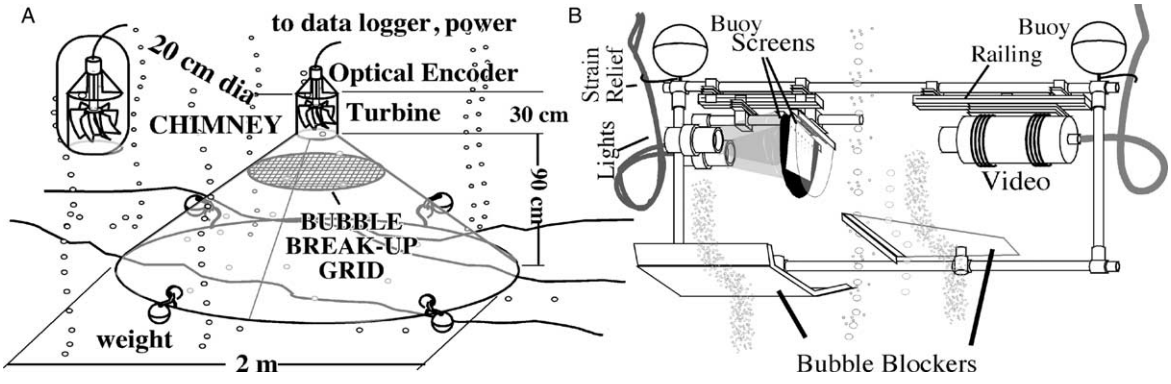

Fig. 3. Schematics of (A) turbine seep-tent, where inset shows turbine details, and (B) bubble measurement system.

Video was acquired at 60 *video fields* s^{-1} and at full digital resolution (720×240 pixels) and extracted to 60 *video frames* s^{-1} (720×240) pixels; in addition, background intensity variations and pixelation noise were also removed. The position, major and minor axes, angle, area, and time were recorded for each bubble. A statistically significant fraction of the bubbles was tracked between frames to determine the bubble vertical, $V_Z(r,t)$, and horizontal velocity, $V_X(t)$, functions. $V_Z(r,t)$ was corrected for camera tilt by calculating the mean trajectory angle, assuming that currents were negligible and that the time-averaged swell was zero.

All bubbles were r and time, t, segregated and histogrammed with logarithmically spaced r-bins to calculate the bubble-size layer-population distribution, $\Psi(r,t)$ (no. $\mu m^{-1}\, m^{-1}$), which was normalized by the radius increment and divided by the number of frames in each t-bin, and normalized to a uniform layer thickness. If only a portion of the stream was observed, $\Psi(r,t)$ was scaled to the entire stream. Bin widths are chosen to optimize statistics near the peak distribution radius. Also, the chosen time width acts as a low pass (block-averaging) filter; thus, wider time bins allow lower frequency trends to be identified better. The $\Psi(r,t)$ is the total bubbles in a metre-thick layer in each size bin and is what sonar observes. The bubble-size emission-population distribution, $\Phi(r,t)$ (no. $\mu m^{-1}\, s^{-1}$), can be calculated from Ψ and $V_z(r)$ and is needed for total flux calculations or to initialize a numerical bubble model. Ψ is not a flux, but is rather the steady-state bubble concentration, and is useful, for example, for calculating acoustic scattering properties, because the speed of sound is dependent upon the volume of gas in the water. This scattering is used by sonar bubble detection approaches (e.g. Vagle and Farmer, 1998). Thus, sonar observations provide a snapshot of the bubbles in the seep bubble stream, but underestimate the seep bubble flux—by a factor of $V_Z(r,t)$.

3. Observations

3.1. Site description

Within the COP seep field, one of the most active seepage areas is Shane Seep. Shane Seep has been the focus of intensive investigations for several years, including bubble and fluid dynamics measurements (Leifer et al., 2000a; Leifer et al., 2003a), oil and tar characterization and microbial community structure (La Montagne et al., 2004), seabed morphological changes (Leifer et al., 2004), geochemical sampling (Clark et al., 2003), flux measurements (Washburn et al., 2001, 2004), and studies of the effect of tar and seepage on fauna (Roy et al., 2003). Flux measurements by a direct capture flux buoy device recorded some of the highest flux values per square metre for the entire COP seep field at Shane Seep (Washburn et al., 2004).

The sediment overburden is Late Quaternary age and <1 m thick for the outer COP seep trends. At Shane Seep the overburden is 2–3 m (Fischer, 1978), consisting primarily of very fine sand with modern total organic carbon of 1–2% (Fischer, 1978). The sand overlies fractured Monterey Formation basement. The upper 30 cm of sand is cemented by tar (La Montagne et al., 2004) and highly cohesive. The seabed near Shane Seep (22-m depth) is also heavily coated with bacterial mats, and large tar balls that are primarily found within the hydrocarbon (HC) or tar volcanoes. These volcanoes are termed hydrocarbon volcanoes rather than mud volcanoes because of their high tar content, which provides the necessary cohesion to form the volcano walls, and fixed vent locations.

3.2. Turbine seep-tent data

SCUBA-equipped divers deployed the turbine tents at Shane Seep on March 11, 2003, as shown in the detailed map of the deployment site, Fig. 4. The N–S and E–W

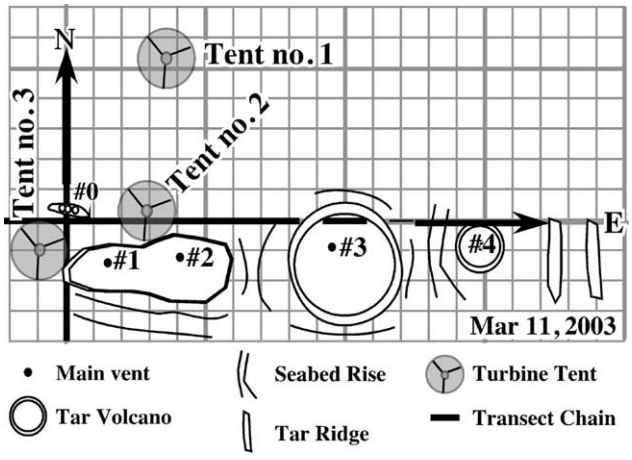

Fig. 4. Seabed turbine seep-tent deployment locations and major features at Shane Seep as measured during a seabed survey. Major vents are numbered 0–4. Major squares are 5 m, minor squares are 1 m. Symbol key on figure.

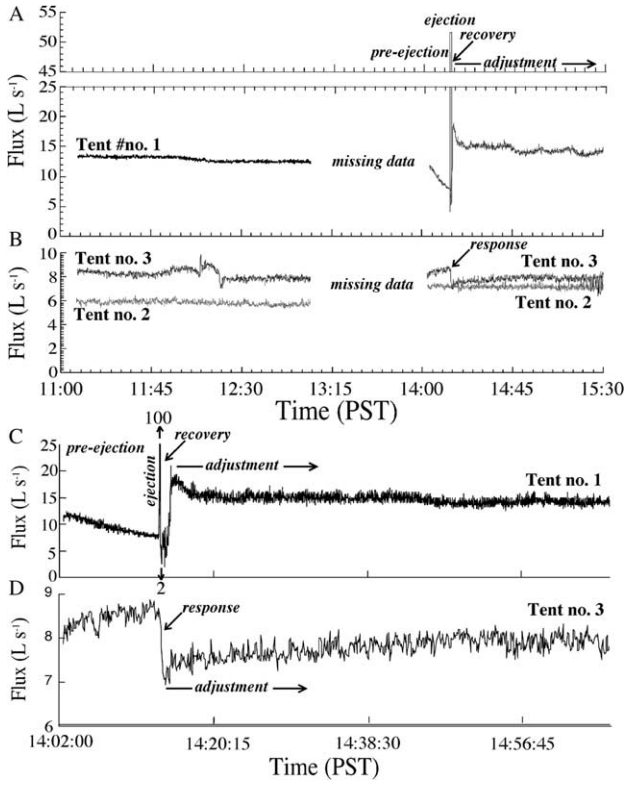

Fig. 5. Flux corrected to standard temperature and pressure for the three turbine seep-tents deployed March 11, 2003. (A) Tent no. 1, (B) Tents no. 2 and no. 3. (C) shows detail of (A) for ejection. Numbers indicate minimum and maximum flux of ejection. (D) Detail for tent no. 3, same time as (C). Tents labeled on figure.

transect chains were laid down the previous year and a spar buoy was attached to a mooring point (several 100 kg) at the intersection of the transect chains. A separate line was connected to a marker buoy at the sea surface. Also shown in Fig. 4 are the major features of Shane Seep observed during a survey that day. These features were noted to change over the previous three years as part of an ongoing seabed survey project reported in Leifer et al. (2004). Changes included the appearance of new HC volcanoes, volcano relocation, caldera wall disappearance and reappearance, and shifting of the dominant seepage vent.

The walls of HC volcanoes nos. 1–3 rose from between 50–100 cm above the seabed, while the caldera floors were approximately at the seabed level. On March 11, 2003, the dominant seepage was through HC volcano no. 3, while volcanoes nos. 1 and 2 were the next most active central seep zones. A very intense, central seep zone was at the mooring point (named HC volcano no. 0) and became the dominant seep zone by the next survey (July 30, 2003). The seabed had risen ~50 cm between volcano no. 3 and volcano no. 4, whose caldera was located on top of a plateau. Two tar ridges were observed further eastward of volcano no. 4 with several minor vents emitting bubble chains from the ridge tops. The tents were deployed in the peripheral seep zone over seepage of varying strengths. Central seep zones were avoided on the concern that fluxes might be too large for the tents, possibly lifting them off the seabed.

The complete data set for the three tents with 5 s running and block time averaging are shown in Fig. 5A and B. The largest flux was at Tent no. 1 and was greater than the other tents combined despite (or perhaps due to) its being located furthest from the main HC volcanoes. The tents began recording data at 1110 Pacific Standard Time (PST), March 11, 2003 until a few minutes before 1300 when the tide shifted and pushed the boat to the other side of Shane Seep, pulling the turbines from their chimneys (as designed). Divers replaced the turbines at about 1400 and data collection continued until worsening weather forced recovery at ~1530. With the tide change, Tent no. 2 may have been shifted slightly. There was a general decreasing trend in the flux in the morning at the three tents, which is consistent with the tidal flux trend variation observed in Boles et al. (2001). Tidal height increased from 19.8 to 20.2 m during the deployment, although this data set was too short to identify tidal time-scale variations. The data also show variations on shorter time scales, including two

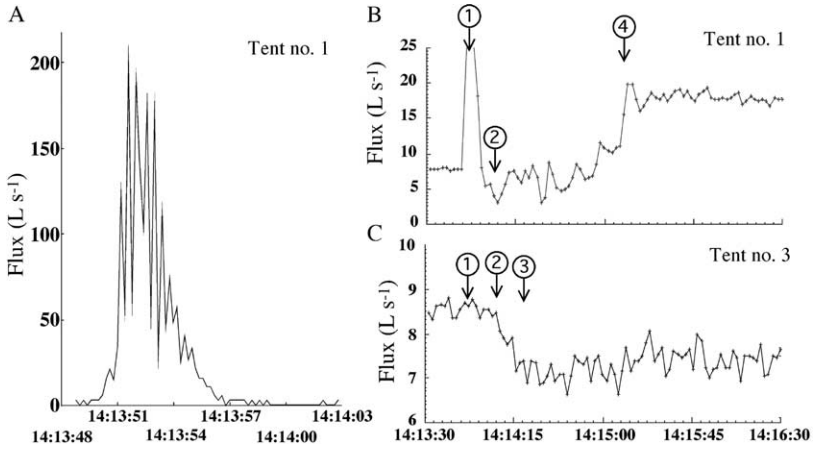

Fig. 6. (A) Unaveraged flux for Tent no. 1 during ejection event. (B) shows the ejection and recovery for Tent no. 1 and the response to the event by flux at Tent no. 3 for 1 s averaging. Note vertical scale on (B) is logarithmic. Tents labeled on figure. Circled numbers are points of note and are described in the text.

transient ejections, one at 1414 at Tent no. 1 and one at 1210 at Tent no. 3. An expanded view of the 1414 ejection at Tent no. 1 and a response at Tent no. 3 are shown in Fig. 5C and D, respectively. Prior to the 1414 ejection, the flux at Tent no. 1 decreased slowly over at least 5 min ('pre-ejection'), while after the ejection, it 'recovered' rapidly to a level higher than originally, before 'adjusting' downward towards fluxes typical before the pre-ejection phase. Meanwhile, the flux at Tent no. 3 responded to the ejection with an abrupt decrease as well as generally trending opposite to the changes in Tent no. 1.

Unaveraged (i.e. raw) data for the 1413 ejection are shown in Fig. 6A. For several minutes before the ejection, the flux from Tent no. 1 decreased (see Fig. 5) and virtually ceased just before the ejection. Then, the flux dramatically increased within two seconds to a peak of $\sim$200 L s^{-1} (at STP). The ejection lasted five seconds and released 0.42 m^3 of gas, then the flux briefly returned to zero. The shape of the flux with time during the ejection was consistent with laboratory produced bubble pulses. These showed an initial flux increase that we interpret as corresponding to the arrival at the turbine of a 'bow wave', $\sim$0.5 s before arrival of the bubble pulse, and a tail lasting one to two seconds due to the upwelling flow following in the bubble pulse's wake. Thus, the ejection likely lasted shorter than 5 s. Unfortunately, the calibration curve had to be extrapolated from lower fluxes because producing a STP flux of 60-L s^{-1} (Shane Seep is at a depth of 22 m) was not feasible in the laboratory. However, given the good correlation of the calibration over three orders of magnitude of flux up to 20 L s^{-1}, we argue that errors in the extrapolation are not significant. Moreover, all the study's steady state flows were within the calibrated range and the precise magnitude of the transient event does not affect the conclusions and discussion.

A longer data subset of the ejection and the flux (time and block averaged to 2 s) shows that flux at Tent no. 1 decreased only temporarily after the ejection (Pt 1, Fig. 6B) before recovering over several minutes to greater than the original value (Pt 4, Fig. 6B). Although, the raw data shows the true minimum flux was 0 L s^{-1}, the averaging scheme artificially increased the minimum (Pt 2 in Fig. 6B). Interestingly, the flux at Tent no. 3 began to decrease (Pt 2, Fig. 6C) $\sim$30 s after the ejection (Pt 1, Fig. 6B). The flux at Tent no. 3 then reached a minimum (Pt 3, Fig. 6C) $\sim$30 s after the minimum for Tent no. 1 (Pt 2, Fig. 6B).

Also visible in the flux of both tents (Fig. 6B) are high frequency oscillations of $\sim$7 s. Based on fourier analysis, Leifer and Boles (2005) concluded that they corresponded to the dominant swell frequency.

Data for the adjustment period (see Fig. 5) are shown in Fig. 7 and provide further support for the hypothesis that vents under Tent no. 1 and Tent no. 3 were connected. For Fig. 7A–C, the running and block time averaging were 10 s.

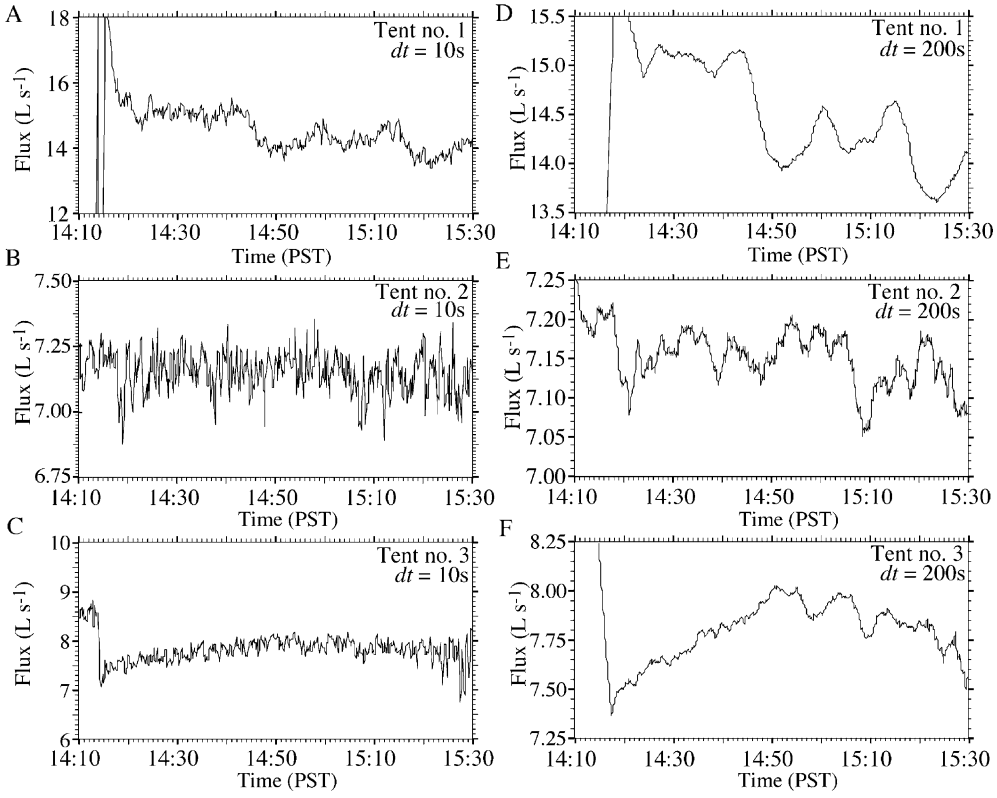

Fig. 7. Temporal record of seep tent fluxes. (A)–(C) Flux was 10 s running average; (D)–(F) flux was 200 s running average. Block averaging, dt, and Tents labeled on figure.

To more clearly see longer trends, 200-s running averages (with 10-s block averages) of the data are shown in Fig. 7D–F. During adjustment, the flux for Tent no. 1 generally decreased, although unevenly. Tent no. 3, showed an inverse trend for the first 30 min post ejection, increasing from a minimum of 7.5 to 8 L s^{-1}, before beginning to decrease. Trends for Tents no. 1 and 3 were also inverse during the pre-ejection period (Fig. 5C to D), when the flux for Tent no. 3 increased while the flux for Tent no. 1 decreased (Fig. 5). Flux for Tent no. 2 was much less variable and also appeared unrelated to the ejection event. For example, for $25 < t < 35$ min post-ejection, standard deviations for (detrended) fluxes were 0.15, 0.06, and 0.12 L s^{-1}, for Tents no. 1, 2, and 3, respectively.

3.3. Seep oil to gas ratio

Oil affects the upward velocity of the gas bubbles in the water column and the migration of gas in subsurface fractures. Alternatively, where oil droplets contain gas bubble(s) or oil coats bubbles, the oil migrates vertically significantly faster through the water column than pure oil droplets (MacDonald et al., 2002). In the subsurface, the lower viscosity translates into a faster migration for gas; thus, it is probable that free gas helps drive the oil through the system by transferring momentum and by pressurizing the system. The gas flow helps drive the oil through the fractures. As a result, there is an intimate interaction between the oil and gas fluxes.

Within the COP seep field, methane fluxes from various seep areas span many orders of magnitude. As a rule, the higher gas flux seeps are visually the least oily both in the slicks formed when each bubble surfaces and bursts, and by the appearance of the oil slicks originating from the various seeps. This visual observation was supported by analysis of oil slick samples. For example, of the informally named inner trend seeps, Shane Seep had the largest gas flux, Farrar Seep (34° 24.109′N, 119° 49.917′W) the lowest, and IV Super Seep (34° 24.090′N, 119° 52.066′W) was intermediate. It was found that the ratio of the lightest alkanes (*n*-C10 to *n*-C12) to *n*-C18 in slick samples—collected by a catamaran oil slick sampler—was the lightest at Shane Seep, the heaviest at Farrar Seep, and intermediate for IV Super Seep (Leifer et al., 2002). If the trends in the ratios of the light to heavy *n*-alkanes can be extended to much lighter *n*-alkanes at these seeps, it would be consistent with the visual observations. Based on these observations we conclude that there exists an inverse relationship between gas flux and oil composition.

Given the very different chemical properties (density, viscosity, etc.) of oil and gas, the fluxes of gas and oil through various fractures is unlikely to be at the same rates; thus, the oil-to-gas ratio should exhibit variability, both spatially and temporally. Seeps provide a mechanism to study this process by allowing the quantity of oil coating a bubble to be measured or inferred—i.e. the oil-to-gas ratio escaping from a vent orifice. In this study, this inference is made based on the changes in the bubble size-distribution with time and the bubble rise-velocity, or hydrodynamics. Interpretation of bubble hydrodynamics requires removing the effects of fluid motions, primarily the upwelling flow, V_{up}. The value of V_{up} was determined from a comparison between the measured bubble vertical-velocities and parameterizations for the rise of clean and dirty bubbles in stagnant water.

3.4. Bubble observations and oiliness

Fig. 8D–F show the vertical velocity, V_Z, for two minor vents and a major vent at Shane Seep. The two minor vents were on the flanks of HC volcano no. 1, while the major vent was the primary vent for HC volcano no. 1. Bubble-size emission-population distributions, Φ, were narrow and sharply peaked for the two minor vents at $r \sim 3500$ and 2200 μm (Fig. 8A and B, respectively). The major vent (Fig. 8C) had a broad Φ including many small (to 200 μm) and large (to 1 cm) bubbles that were emitted in pulses. Also shown are polynomial, least-squares fits to the data, and the clean and dirty bubble rise-velocity parameterizations, V_B, based on a review of laboratory experiments by Clift et al. (1978), corrected to 13 °C (Leifer et al., 2000b). Bubbles more than two standard deviations from the fit were considered outliers and are indicated by diamonds. For all plumes, V_Z was clearly elevated above the stagnant water V_B. This was due to the upwelling flow that accompanies rising bubble streams. Upwelling flows for COP bubble streams spanning a wide range of gas fluxes were quantified in Leifer et al. (2000a) and Clark et al. (2003). The upwelling flow velocity, V_{up}, can be calculated from bubble rise speed by:

$$V_z(r,t) = V_{up}(t,\Phi) + V_B(r,s,p) \quad (2)$$

where V_B varies with bubble radius, r, s is the presence or absence of surfactants, and p is the oil-to-gas ratio. We assume V_{up} is spatially homogeneous within the plume but can vary with t due to variations in Φ (as shown in data below). Assuming spatial homogeneity is a simplification. McDougal (1978) showed that spatially, V_{up} is Gaussian and extends beyond the edge of the rising bubbles. Turbulence introduces variability into V_{up}, but not when time averaged. The effect of p on V_B is unknown. Depending on the oil-to-gas ratio, the effect can be primarily due to a decrease in buoyancy (high p), or by changing the bubble hydrodynamics (low p) more than the effect of oceanic surfactants, discussed in the next paragraph. Due to insufficient data, no attempt is made in this manuscript to calculate p; however, some of the variability in V_z can only be explained by widely different values of p. Solving for V_{up} in Eq. (2) for the minor vents (Fig. 8D and E), V_{up} yielded either ~ 10 or ~ 15 cm s^{-1} for the minor vents, depending upon whether s was clean or dirty. V_{up} for the major vent was much faster (~ 50 cm s^{-1}) than the minor vents. Due to turbulence and

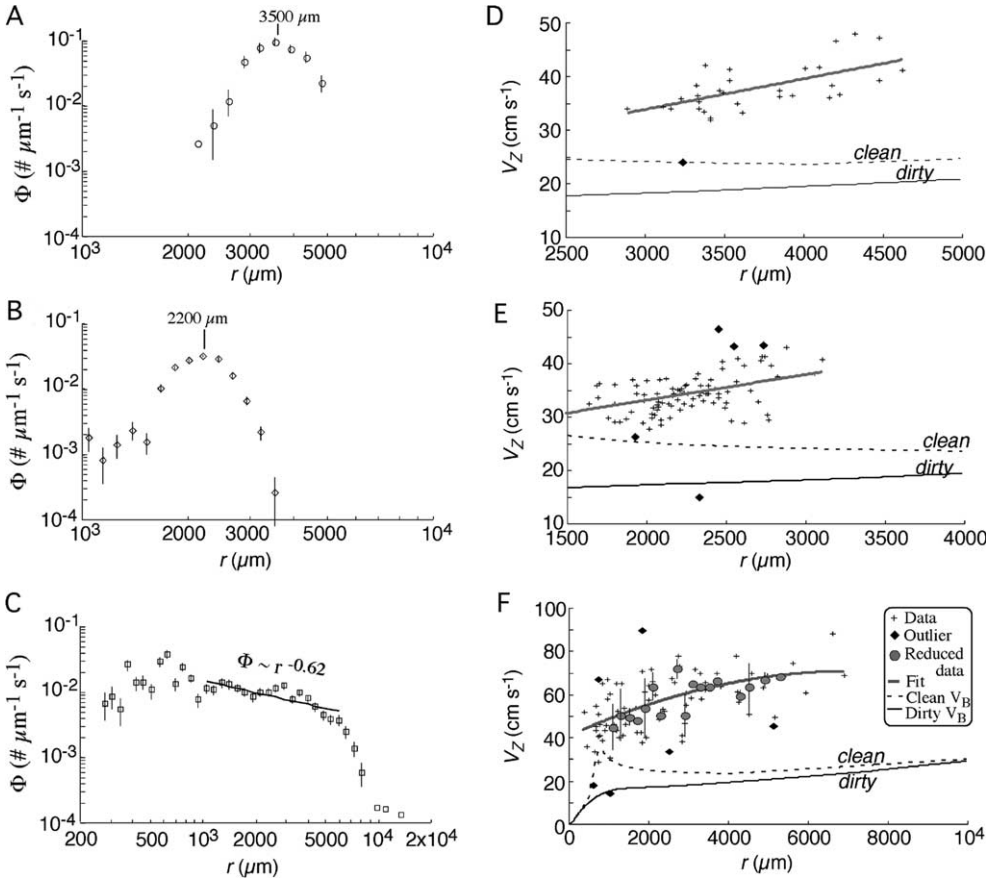

Fig. 8. Bubble flux distributions, Φ, versus radius, *r*, for (A and B) two minor vents and (C) a major vent, including least squares fit to data for the major vent plume. (D–F) Vertical velocity, V_Z, versus *r* for vents in (A–C). Also shown are the clean and dirty bubble rise velocity parameterizations in stagnant water and least squares fit to the data. Data key on figure.

pulsing of Φ for the major vent, there was significant scatter in V_z. Thus, bubble velocities were averaged in 250-μm radius bins and are shown as circles in Fig. 8F.

Determination of V_{up} requires knowing the buoyancy retardation effects due to oil and the bubble surface cleanliness. We approach this analysis by assuming all bubbles are oily, but most bubbles have insufficient oil contamination to affect buoyancy. The question of bubble cleanliness is non-trivial for these large bubbles. Patro et al. (2002) showed that bubbles larger than 700 μm behave clean in seawater. The explanation lies in the stagnant-film cap model, in which the flow pushes the surfactants to the bubble's downstream pole, leaving most of the bubble surface surfactant free (Sadhal and Johnson, 1983). The same process may occur with oily bubbles. One approach to infer the bubble surface state is to look at the bubble trajectory and shape oscillations as a function of *r* (e.g. Patro et al., 2002). The clean bubble V_B-parameterization increases with *r* until the onset of oscillations causes a peak at ~700 μm, above which V_B decreases with *r* due to the trajectory oscillations (Leifer et al., 2000b), shown by the dashed line in Fig. 8F. In contrast, the dirty bubble V_B-parameterization does not exhibit a sharp transition to oscillations and thus has no peak at 700 μm (shown by thin black line in Fig. 8F). For the major vent, if we assume all bubbles were clean, the calculated V_{up} varied between 40 cm s^{-1} for the largest bubbles and 10 cm s^{-1} at 700 μm (i.e. an estimated V_{up} less than for the minor vents). If we assume all bubbles were dirty, the calculated V_{up} is a more consistent 45 cm s^{-1} for the largest bubbles, and 35 cm s^{-1} for the smallest.

Bubbles with V_Z more than 2 standard deviations from the fit were classified as outliers and not used in the fit. For example, in Fig. 8D, a 3200-μm radius bubble had V_Z of only 25 cm s^{-1}. One possibility is that this bubble was trapped in a turbulence eddy. However, examination of the video showed it to be rising much slower than other nearby bubbles, i.e. its trajectory was significantly shallower, and there was no evidence of erratic (turbulent) motions. A similarly slow moving, 2300-μm bubble was tracked in the second minor vent plume (Fig. 8E). Its velocity also could not be explained by turbulence. Several abnormally slow-moving bubbles also were tracked for the major vent. They were primarily small and their velocities could not be explained by turbulence. An image sequence for the major vent is shown in Fig. 9 and provides an example of these very slow bubbles rising amongst many larger and faster moving bubbles. The locations of three small 'bubbles' or gas containing oil droplets (*r*~600–700 μm) are indicated

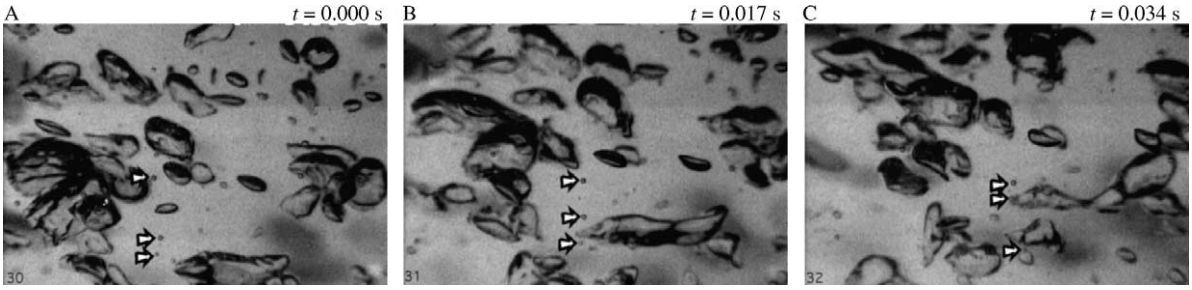

Fig. 9. Video image sequence of bubbles in the bubble stream from the major Vent no. 1 shown in Fig. 4. The bubble distribution for the vent is shown in Fig. 8C. Three oily bubbles are indicated by arrows. Time relative to frame (A), *t*, shown in images. Vertical ticks in upper portion of images are 1 cm apart and vertical is tilted 15° clockwise. Aside from vertical ticks in the upper portion of the image (1 cm apart), everything in the field of view is a bubble.

by arrows. They clearly were rising much slower than most other nearby bubbles, but too fast to be pure oil droplets. Most bubbles rose ~1/4 the frame height (~4 cm) between frames, while these three bubbles barely rose, despite the strong upwelling flow. Instead, they primarily drifted in the current. The most plausible explanation is that these bubbles had a thick oil coating that reduced their buoyancy. That these were bubbles is shown by their white centres, indicating they were gas filled.

The data in Fig. 8 and images in Fig. 9 show that the oil to gas ratio was highly variable. Thus, while some small bubbles were very oily, others of the same size were not. Furthermore, the oil–gas ratio at the seabed is unlikely to remain the same throughout the water column; it may change rapidly due to fractionation from bubble breakup, as well as other bubble processes such as decreasing hydrostatic pressure and gas exchange. Since bubble breakup only was observed for the major vent, our approach of studying bubble hydrodynamics to infer seabed oil to gas ratios is best applied to minor-vent bubble streams, as close to the seabed as feasible.

The layer, bubble-size population distribution, $\Psi(r,t)$, (no. $\mu m^{-1}\, m^{-1}$) for a third minor vent in the southeast peripheral zone is shown in Fig. 10A. Its spectral peak half-width was only ~100 μm, where the half-width was the difference between the two radii where Ψ was $1/e$ times the peak value. To reduce noise, Ψ was 1-s running averaged, which caused single bubbles to appear as rectangles. Temporal variability both in peak radius, r_p, and distribution half-width is apparent in Fig. 10A. Trends in r_p are more clear in Fig. 10B, which shows $r_p(t)$ with running averages of 0.083 and 1.0 s. The time series for r_p shows an oscillation of ~4 cycles per second and several slower trends. Specifically, r_p slowly increased until ~2.5 s, then decreased until ~4.75 s, and finally increased until the end of the data set. These changes in r_p were generally the same as trends in the total volume (Fig. 10C), but the correlation was low ($R^2 = 0.45$). Since the total volume is simply $\int\{\Psi(r,t)4/3\pi r^3\}dr$, the poor correlation between the two series must result from changes in the shape of $\Psi(r,t)$, not just changes in r_p.

Bubble size produced from a vent is controlled by several factors. The primary control is vent-mouth diameter, but also gas flux, horizontal water velocity, surfactant contamination, and oiliness play a role, illustrated schematically in Fig. 11. Given the lack of published data, we make the simplifying assumption that for oil-coated bubbles in seawater, surfactants do not have a significant effect beyond that of the oil. For the low flux of these vents and stagnant water, bubble size is independent of gas flux (Marmur and Rubin, 1976) and bubble size depends solely upon vent-mouth diameter (Blanchard and Syzdek, 1977). Thus, flux changes only cause changes in the bubble emission rate.

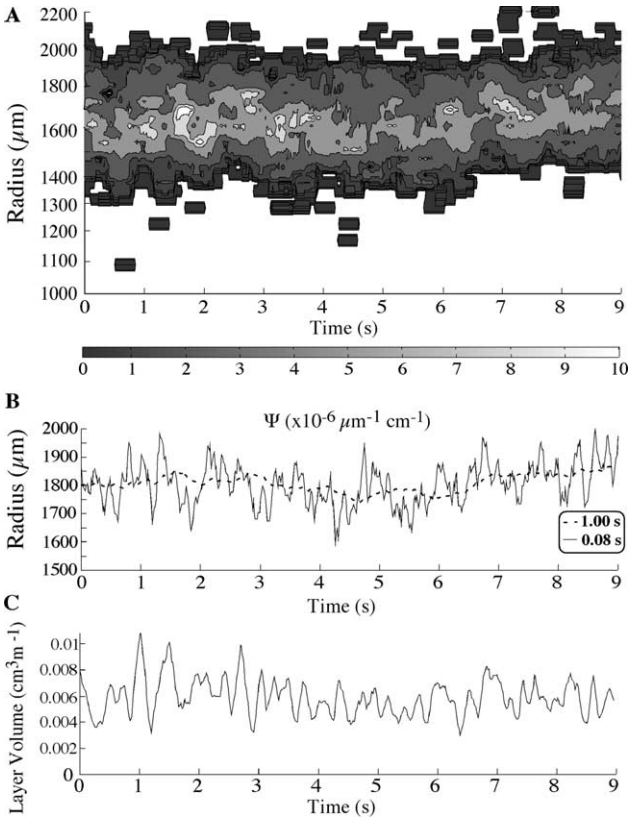

Fig. 10. (A) Contour plot of time and radius variations in the layer bubble-population size-distribution, Ψ, for a single minor vent in the peripheral zone (southeast). Key to population levels below figure. (B) Peak radius of distribution versus time for 1 s and 0.083 s running averages. Data key on figure. (C) Total plume volume in a 1-m layer versus time. See text for details.

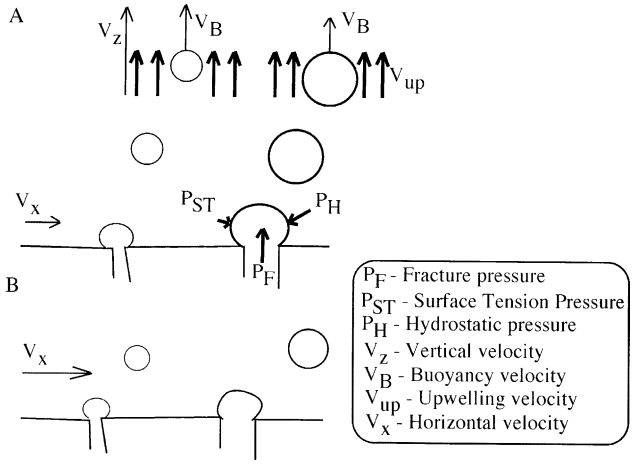

Fig. 11. Schematic showing fluid velocities associated with and affecting bubble formation, for low (A) and high (B) horizontal velocity, V_X. At higher V_X, bubbles are smaller, although the amount the bubble size is reduced varies depending on bubble size. Symbols defined on figure.

Another factor that can affect r is horizontal flow, V_X, due to swell, currents, etc., across the vent mouth. At high V_X, the emitted bubble size decreases, while for low V_X there is negligible effect. Furthermore, the dependence of r on V_X is also size dependent—i.e. $r = F(V_X, r)$ (Tsuge et al., 1981). Finally, when oil and gas flow through a vent, the oil coats the vent mouth. Thus, we propose that oil flux variations produce variations in oil coating of the vent mouth and thus a variation in vent mouth diameter and hence r. The relative importance of these parameters to bubble size can be determined by comparing the trends in r with trends in V_X, V_Z, and V_B (V_B is the buoyant rise velocity in stagnant water—see Fig. 8F for parameterizations).

The calculated V_{up}, for all tracked bubbles in Fig. 10A is shown in Fig. 12A and assumed dirty bubbles. During the first 3.25 s, V_{up} decreased significantly, from ~25 to

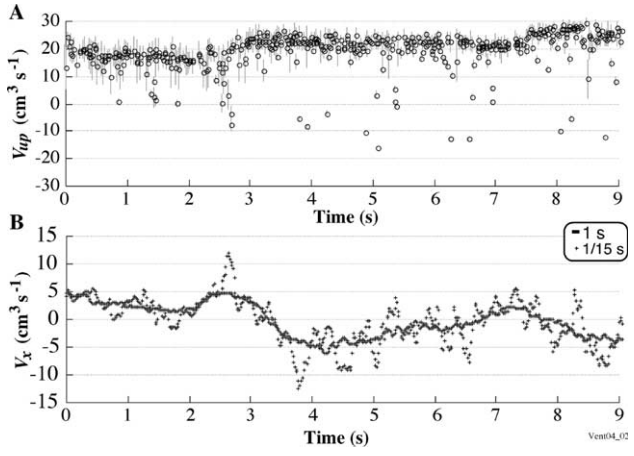

Fig. 12. (A) Upwelling velocity, V_{up}, versus time for all tracked bubbles. Vertical lines show error of 1 std. (B) Running-averaged horizontal velocity, V_X, versus time for bubble stream shown in Fig. 10. See text for details on calculation of V_{up}. Running average of V_X was 1/15 and 1 s. Data key on figure.

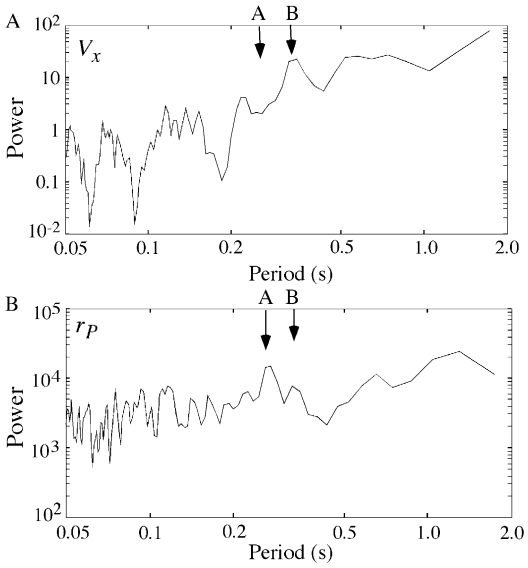

Fig. 13. (A) Power spectrum for horizontal water velocity, V_X, and (B) power spectrum for peak radius, r_P, for the time series shown in Fig. 10B and 12B. Arrow in A shows peak in r_P spectrum.

~12 cm s^{-1} before suddenly jumping to ~20 cm s^{-1}. V_{up} then remained roughly constant until $t = 8$ s when it abruptly increased to ~25 cm s^{-1}. There also were several times when the calculated V_{up} decreased significantly and transiently (transient is defined as a period of 0.25–0.5 s)—e.g. at $t = 2.75$ or 5.1 s. Due to fluid inertia, it is unlikely that such transient decreases in V_{up} were real; instead, these decreases in V_{up} probably represented decreases in bubble V_B due to increases in bubble oiliness. V_X for both 1/6 s (10 video fields) and one second (60 video fields) running averages are shown in Fig. 12B. Although there was no clear relationship between V_X and V_{up}, transient decreases in V_{up} appear associated with peaks in V_X ('puffs'). It is also interesting that right before the sudden jump in V_{up} at $t = 2.75$ s there was the largest puff (peak in V_X). Since V_{up} is related to the magnitude of the bubble flux and the bubble size-distribution, this suggests that V_{up} could be affected by V_X, either by changes in r or the total bubble flux.

Evidence that the variations in r were not driven by changes in V_X is shown by a comparison between the power spectra for detrended r_P and V_X, shown in Fig. 13. Spectra were calculated with a Blackman window and a 256-point FFT with 25% overlap. The r_P spectrum showed a strong and well-defined peak at a period of ~0.25 s with two side lobes and a second strong peak at ~0.12 s. The spectrum for V_X had a local minimum at 0.25 s and a peak at 0.4 s, where r_P instead had a minimum. The dissimilarity of these two spectra strongly argues that V_X was not an important parameter driving the variations in r_P. Therefore we propose that variations in r_P were due to variations in bubble oiliness, or equivalently, changes in the oil to gas ratio.

4. Discussion

There is considerable subsurface interconnectivity and complexity in the linkage between seepage at different locations in a seep area. The data also showed high-flux transient events were preceded and followed by an absence of flux, and subsequently, recovery to greater flux than before the event. Moreover, the flux recovery was in quasi-discrete steps. To explain the ejection behaviour, a fracture oil deposition model was proposed by Leifer et al. (2003a). This model proposed a mechanism for clogging of fractures that then induce ejection events. However, this conceptual model did not address the observed interconnectivity, nor did it provide insight towards the ultimate goal: numerical model development. Thus, we present below an electrical model analog for oil and gas migration in a fractured network. A more detailed description of the fracture deposition model than Leifer et al. (2003a) is presented afterwards.

4.1. Electrical flow model

Seep features are interconnected in an extremely complex manner through subsurface fractures, faults, and sediment. Due to this interconnectedness, variations in seepage at different locations are related to each other, although the effect decreases with distance due to the flow resistance within the seep pathways. Thus, a simplified but useful approach is to model seepage as a network of interconnected resistors (representing viscosity) and capacitors (representing fracture capacity) driven by a voltage potential, V_R, (representing fracture overpressure; Fig. 14). The total flux, or current, i, is split through the different resistors or pathways. Each pathway has a volume, which acts as a capacitor. Thus, an increase in resistance along one pathway, say R_1, affects the current through all other pathways, particularly closer ones since there is less resistance against a shift in the current flow between R_1 and R_2 than between R_1 and R_3. This shift is termed readjustment. Although it may seem that readjustment maintains constant total flux ($i = i_1 + i_2 + i_3$), the total system resistance is increased. In addition, the increased flow through R_2 causes higher frictional damping (akin to increased resistance due to heating) that increases R_2 among others, thereby decreasing i. The capacitance of the system has the effect of a low pass filtre, thus transient changes are 'buffered' by the capacitance of the network. V_E represents the pressure necessary for the escape of a bubble (hydrostatic plus surface tension) into the ocean. If the system is externally forced, V_E varies with t, where t is time, due to factors such as tidal hydrostatic-pressure changes, the response from each pathway differs depending upon its resistance and capacitance. In addition, we can consider external forcing and transient events as probes of the network morphology. Within each pathway, most of the resistance occurs at narrow, points or bottlenecks. Our model is appropriate only for these, narrow rate-limiting portions of the fractures and not for larger portions of the fracture.

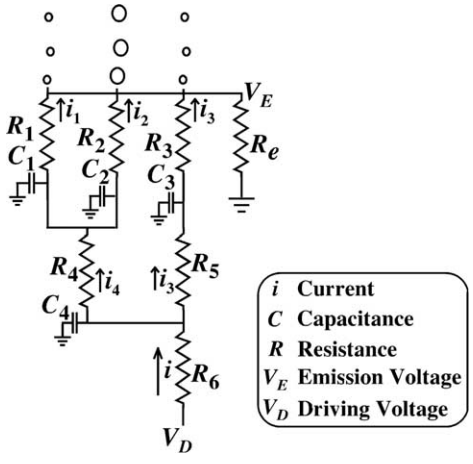

Fig. 14. Schematic for an electrical model of a seep fracture network. Symbol key on figure. See text for more details.

Despite containing considerable complexity, this model is highly simplified. The largest simplification is that it only considers a single phase. One could design separate models, one for each phase (gas, oil, water, and tar). However, one would be neglecting the interaction between phases (interpermeability). For example, an increase in the gas flux increases the oil flux (by increasing the driving force, i.e. V_D). It is as if there were multiple, parallel, but different, networks (resistance of oil is much greater than for gas) with the value of each component dependent upon the value of the comparable component in the other network. The linkage between the phases is intimate with numerous feedbacks. As an example, consider the effect of an increase in gas flow in a fracture. This increases the oil flux in the fracture since the gas flow drives (a drag effect) the oil flow. Greater oil flow fills the fractures at bottlenecks, increasing the resistance to gas flow and thus decreasing the gas flow. This leads to an decrease in the pressure driving the oil. When oil flow is higher, the locally available quantity of oil decreases (drains the capacitor), leading to a lower flow of oil. This increases the gas flux, which replenishes the local oil 'reservoir' from deeper in the fracture system. Thus, many of these feedbacks can easily lead to oscillatory cycles.

Although for this paper we consider the oil, gas, and tar as three separate phases, the reality is that there is a spectrum spanning the range of chemical properties, such as viscosity, density, etc. Furthermore, the different hydrocarbon components respond differently to the gas forcing (i.e. the lighter and less viscous components are driven faster by the gas flow and overpressure than the heavier and more viscous components).

Another simplification is that we largely neglect a fourth phase, water, not because it is unimportant, but because our measurement approaches are unable to quantify the water

flux associated with the oil and gas flows. The portions of the fractures that we are modeling are narrow enough that bubbles are in frequent contact with the walls, rather than open pipes. In open pipes, water can pass around the rising bubbles and the dominant driving force is buoyancy. As a result, the flow is fast and therefore the resistance is less. In the narrower fractures, the gas voids (bubbles) fill the space, and are surrounded by a thin film of water. In this case, the water cannot flow around the bubble, and thus is forced upwards by local overpressure (exsolution, discussed below) relative to local hydrostatic. This is similar to gas flow through a glass capillary tube. As a result, the buoyancy force is unimportant compared to surface tension forces. Compared to the resistance of flow through a narrow fracture, the flow in an open, pipe-like fracture is significantly less. Thus, if we consider a narrow and a wide fracture as two resistors in series, the total resistance is approximately that of the higher resistance portions. In contrast, due to its larger volume, the more open portions of the fracture may dominant the capacitance of the two fractures.

Another important (and probably critical) process neglected in our simplified model is that water allows the gas to change from dissolved to gaseous form. This provides an overpressure that can drive bubbles through the fractures despite that capillary force will strongly adhere bubbles to the fracture walls. The exsolution of the gas phase has been proposed to explain fluid eruptions in a geothermal well where the water is gas saturated (Heiko Woith, Geo-Forschungs Zentrum, Potsdam, Germany, personal communication, 2003). Exsolution was observed at a beach seep (Summerland, California) where oil escaping through the sand developed small bubbles as it flowed down the beach (Ken Wilson, Calif. Dept. Fish and Game, Santa Barbara, CA, personal communication, 2003). Assume that at some depth the water in the fracture system is in equilibrium with the dissolved phase. As this fluid rises (driven by bubbles or other geofluid processes) it becomes supersaturated relative to the decreasing hydrostatic pressure. As a result, the gas exsolves and forms bubbles or grows existing bubbles. The gas pressure also increases relative to the fluid as the bubble rises due to the decreasing hydrostatic pressure. Since the gas cannot expand (due to the fracture walls), exsolution increases the upward pressure, which further drives the upward migration of hydrocarbons (and presumably water). However, we argue that the resistance is dominated not by the low resistance portions of the fractures but by the narrow portions.

4.2. Fracture oil deposition model

The fracture oil deposition model is shown schematically in Fig. 15, Inset A. This model requires narrow fractures where the rising gas bubbles continuously touch one or more fracture walls. In larger portions of the fracture system where bubbles rise freely, the resistance is much less than in

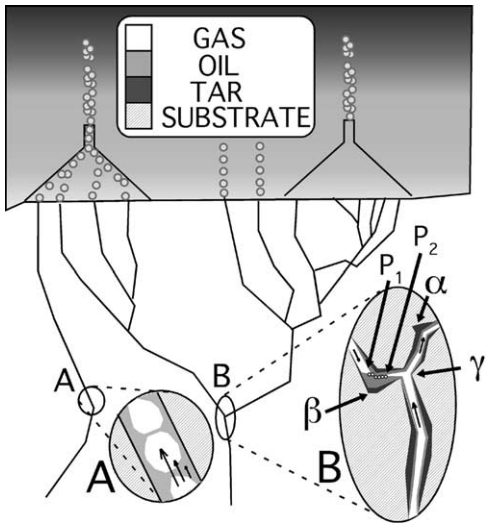

Fig. 15. Schematic illustrating proposed oil regulator mechanism for hydrocarbon migration to the sea floor. Inset (A) shows oil and gas flowing through a fracture. Inset (B) shows oil regulator model. Data key on figure. See text for explanation.

the narrow portions, and as discussed previously, it is the narrow flow sections that control the fracture resistance. However, even in the larger fractures, wherever tar globules are attached to walls, oily bubbles will deposit oil on these tar patches, although in water-wet reservoirs, the non-tar surfaces are water coated and unavailable for oil deposition.

We simplify the following discussion by neglecting complicating effects of water. In the narrow fractures, gas flows primarily in the fracture centre, while the walls are oil coated due to the bubbles forcing the oil against the walls. The gas flow drives oil along the walls and thus the oil flow increases with distance from the walls. At the fracture walls, continuity demands that the velocity goes to zero, thus there is a boundary layer of immobile oil. As this oil degrades due to physical, chemical, or biological processes, it becomes more viscous and less mobile until it becomes immobile tar on the fracture wall. This tar has now created a narrower fracture opening, i.e. the fracture progressively clogs. The clogging increases the resistance (R), decreasing the flow (i) and thus increasing the pressure drop (V) across the blockage until the pressure across a narrow point (a bottle neck) blows clear the tar.

Tar migration can also block fractures. For example, a small quantity of tar migrating up from below can seal a fracture (again most likely at a bottleneck), first leading to a rapid cessation of seepage, until the resultant pressure rises and blows clear the tar blockage. A tar blockage bottleneck is shown at position α in Fig. 15, Inset B, and is the most likely explanation for the ejection observed by one of the seep tents (Fig. 5). In this model, the violence of the tar blow-through also frees tar deposited on the fracture walls at the bottleneck and elsewhere, decreasing flow resistance in the fracture and hence leading to an increase in the flux (akin to ‘cleaning the pipes’ in a house). The increased gas

flux drives an increased oil flux that slowly fills in the now more open fracture. Tar loosened by the ejection can break free and lodge at shallower bottlenecks in the fracture system. Thus, the expected flux pattern (e.g. Fig. 5, Tent no. 1; or Fig. 7D) is a rapid and approximately exponential decrease in flux as the fractures are sealed at a bottleneck and the shallower fracture network portions depressurize. After the initial blow-through, deeper portions of the fracture system than the bottleneck act as a reservoir that is rapidly depressurized by the event, causing a dramatic decrease in flux. Subsequently, gas arrives from deeper than the bottleneck in the fracture system, restoring the gas flux to a higher level than initially since there now is less resistance in the more open fracture. However, the blow-through releases tar (and oil and gas) into the fracture system; the tar lodges at shallower bottlenecks, leading to abrupt decreases in flux in other locations. This tar may then blow through or be pushed against the walls, re-opening the fracture. In either case, a new equilibrium at a lower flux is established.

The depressurization phase leads to decreased flux through other, closely connected fractures. Subsequently, the increased flow through the ejection fracture (where resistance has decreased) also causes a decreased flux through other, closely connected, fractures; hence, the inverse seepage trends with other tents. The negligible response of Tent no. 2 to the ejection at Tent no. 1 strongly suggests that its connectivity with Tent no. 1 was of much greater resistance than between Tents no. 1 and 3. Thus the seepage at Tent no. 2 was predominantly through fractures largely independent of the other tents. Higher resistance may arise through greater distance, narrower fractures, more oily fractures, or some combination.

However, the deposition mechanism cannot explain the observed time delay of $\sim$20 s for the response of Tent no. 3 to the ejection at Tent no. 1 (Fig. 6). The simplest assumption is that the delay results from the transport time between the fracture interconnection point (Fig. 15, Inset B, γ), and the seabed. From the flux at Tent no. 1 and the delay time, and assuming a mean fracture cross section of 1 mm^2, a subsurface distance from Tent no. 3 to 1 can be calculated. For the flux of 7.5-L s^{-1}, the gas volume fluxed during the 20-s delay was 450 L (at STP), corresponding to a distance many orders of magnitude greater than the separation between tents. This distance shrinks if hydrostatic pressure was considered or if the mean fracture cross section was 1 cm^2, but still remains unreasonably large. This implies the mean cross section for the shallow subsurface 'reservoir' depressurized by the ejection must have been much larger than 1 cm^2.

Importantly, Tent no. 3 did not show an exponential decrease during this initial 20-s period, as one would expect for a draining reservoir. Instead, the flux remained approximately constant during this period. Only afterwards was an exponential decrease observed in Tent no. 3, with the flux dropping to almost zero.

Thus, we propose adding a regulation mechanism to the fracture deposition model, shown schematically in Fig. 15, Inset B. This mechanism was suggested by the similarity of the field data after the ejection to the behaviour during tent calibration experiments when the compressor pressure dropped below that necessary for regulation. While regulated, the flow through the bubble frets remains constant, but once the pressure across the regulator drops too low, the flow rapidly decreases, similarly to what was observed for Tent no. 3. We propose that an oil-tar seal can act as a natural regulator, shown in Fig. 15, Inset B, at β, where a fracture opening is oil filled. The pressure at P_2 is greater than P_1, and the gas forces itself through the viscous oil as bubbles. Regulation occurs when the pressure difference across the reservoir, P_2–P_1, affects the reservoir. If P_2 increases, the oil is pushed further into the fracture, which becomes narrower. Thus, the gas must pass through more oil, and through the narrower portions of the oil filled fracture. This increases the flow resistance, thereby regulating the flux. However, in the case of an ejection, P_2 decreases rapidly. As long as $P_2 > P_1$, the flow continues, but once $P_2 < P_1$, the oil flows backwards. During the ejection, P_2 must have decreased to almost zero (since the flux decreased to zero), $P_2 \ll P_1$, and thus oil would have back-flushed through β until there was a clear path for gas to forward flow through β. Once that happens, P_1 would very rapidly decrease, venting through the pathways to Tent no. 1. This oil regulator mechanism is hypothetical and there are many other possible regulator mechanisms that could occur in an oil-tar-gas system. For example, compression of semi-elastic tar due to an increase in P_2–P_1 would more completely fill the fracture, preventing a concomitant increase in flux.

Our model was developed to explain observations on near seabed hydrocarbon migration. These seeps are ultimately fed by migration along faults and fractures from kilometre depth reservoirs. The conceptual model presented here can be applied to deeper portions of the migration if pressure dependent chemical and physical properties of oil and gas are accounted for (e.g. gas solubility).

4.3. Gas/oil migration and bubble oiliness

The bubble observations showed a change in bubble size from a single minor vent. However, bubble size is related to vent diameter for the low flow rates of the minor vents, not gas flux. As a result, increased flux simply causes a higher bubble emission rate (Marmur and Rubin, 1976). Water flow across the vent mouth (e.g. from swell, currents) decreases the emitted bubble size, but the effect also is negligible for low flux, (see the schematic in Fig. 11). During some periods when horizontal velocity (V_X) decreased (e.g. Fig. 12, 0 s $< t <$ 2 s) peak bubble size (r_P) decreased (e.g., Fig. 10B —note that there is a time lag of $\sim$0.5 s between the emission of a bubble at the vent

and its arrival in the camera field of view—while horizontal velocity, V_X, variations are simultaneous with depth. In contrast, during other periods an increase in peak radius, r_P, ($6<t<9$ s) corresponded to a period of no significant trend in V_X. From this we concluded that most of the variation in r_P cannot be explained by variations in V_X (supported by the differences between spectra for V_X and r_P—Fig. 13). Thus, we concluded that the effective vent mouth size varied due to the oil flux, or more specifically, that not only the gas flux but also the gas-driven oil flux, varied with time and, therefore, the thickness of the oil coating on the fracture walls also varied with time. As a result, smaller bubbles are formed when the oil flux is greatest and the effective vent mouth smallest; larger bubbles are formed when the oil flux is least and the effective vent mouth greatest. In other words, bubble size and gas flux are inversely related to oil flux.

Although external forcing probably plays a role in the variability in the oil–gas ratio and fluxes—e.g. swell influences gas flux (Leifer and Boles, 2005)—much of the variability, particularly on time scales shorter than the dominant swell period, ~7 s (Leifer and Boles, 2005), probably is explained by the interaction between oil and gas fluxes in the subsurface fractures. For example, when there is greater oil flux, the resistance is greater and the gas flux is less. The decrease in oil flux then causes a buildup of oil that decreases the gas flux, but increases the pressure difference across the buildup. This increased pressure drives the oil faster, clearing the blockage. As the blockage clears, the gas flux rises. The increased gas flux increases the oil flux from deeper in the fracture system, once again starting to block the fracture. As the fracture begins to block, the gas flux decreases and the oil builds up, repeating the cycle. Thus, the inferred relationship between oil and gas fluxes is consistent with this proposed interplay between oil and gas. For the major bubble vent, a strong oscillation in gas flux was observed at ~4 hz. These observations also are consistent with the observed oil-to-gas ratios at the various seeps, namely that seeps with high gas fluxes have low oil fluxes, while seeps with high oil fluxes have low gas fluxes.

The transient decreases in V_{up} with puffs or peaks in V_X, strongly implies that for rapid increases in V_X, oilier bubbles were emitted, or equivalently, that the oil flux temporarily increased. In this explanation, the puff at 3 s in Fig. 12B, may have removed a droplet of oil that allowed subsequent bubbles to be cleaner and rise faster, since there was no significant change in r_P or layer volume at 3 s (Figs. 10B and C). The absence of low V_{up}, or very oily bubbles (Fig. 9), in the data series is not critical to this hypothesis since V_{up} was calculated only from 'tracked' bubbles, ~10% of the bubbles emitted (although all were analyzed for Ψ).

The observed very oily bubbles (Fig. 9) must have been formed by one of two mechanisms, either at or below the vent, or in the water column by bubble breakup. Since bubble breakup was not observed for the minor vents, it must have occurred at the vent mouth. For the major vent, the very large bubbles were observed breaking up into many small bubbles from their trailing edge. Since oil is a surfactant, and surfactants are pushed to the bubble's downstream hemisphere (Sadhal and Johnson, 1983), oil is also likely pushed to the bubble trailing hemisphere. Thus, some of the bubbles breaking off the trailing bubble edge probably acquire a heavy oil coating of oil. This also explains why V_{up} for the smallest bubbles in the pulsing plume was the lowest, i.e. they were the oiliest.

One implication of this observation is a bifurcation of the plume with very oily bubbles, perhaps better described as gassy oil-droplets, rising much slower and thus drifting further down current, while the majority of the significantly less oily bubbles rise nearly vertically. This implies two different fates for these oily bubbles, with the majority of the slick forming downcurrent of the bubble plume.

4.4. Limits of the approach and models

The approach and models discussed in this study were for seepage through vents and fractures that remain fixed over long time scales. In cases where the sediment is unconsolidated, the mechanism of bubble rise through the sediment is very different from migration through fractures; thus it is unlikely to exhibit similar interconnectedness, and approaches outlined herein are inappropriate. Seep migration through unconsolidated sediment does not have permanently open pathways and, thus, is similar to sediment ebullition in which bubbles migrate via 'elastic failure' (Johnson et al., 2002). This mechanism is likely to produce a random or quasi-random emission temporal and spatial distribution. A third exception is brine pools (MacDonald et al., 2000), where the apparent seabed is a (denser) fluid. For a brine pool, additional complexities arise from bubble-fluid processes in the brine pool, such as gas exchange, similar to bubble processes in the water column (Leifer et al., 2000a).

5. Conclusions

Data were presented from the test deployment of three turbine seep-tents and a bubble measurement system. Based on observations of seepage at three tents during an ejection event in the period immediately afterwards, a conceptual model was proposed. Partially filled fractures act as regulators. Oil deposition on the fracture walls progressively clogs the fracture until pressure buildup causes a blow-through. Fractures are also clogged by tar migration. An electrical network model was used to describe the behaviour of a seep network. The model predicts that the effect of ejections is not simply flux readjustment between fractures, but also a change in the total fracture network resistance, altering the total flux.

Although there appeared to be a strong correlation between the ejection event at Tent no. 1 and flux changes at

Tent no. 3, this relationship is probably not predictive. Thus, subsequent ejections at Tent no. 1 may or may not cause a reaction at Tent no. 3. However, the model predicts there is likely to be a reaction at some locations in the seep area. Bubble observations were used to infer that the oil and gas fluxes were inversely related; higher oil flux decreases the fracture size (increasing resistance) causing lower gas flux. This relationship between the two phases is likely to induce oscillations. For the major vent studied there was a strong oscillation with a period of 0.25 s.

Both minor and major vent bubble streams were observed to produce infrequently bubbles with very low rise-velocities that were interpreted as being very oily. These very oily bubbles likely follow distinct trajectories from the majority of bubbles in the plume, leading to the formation of two surface slicks, with the majority of oil surfacing downcurrent of the bubble plume.

The data demonstrate the importance of collecting simultaneous flux measurements at multiple locations for interpretation of the data, and on a range of time scales. Finally, the presented data show the importance of long-term monitoring to quantify the contribution of marine hydrocarbon seepage to global budgets by incorporating the transient input; however, because of seep readjustment, monitoring at multiple locations is also critical.

Acknowledgements

We would like to thank the support of the US Mineral Management Service, Agency no. 1435-01-00-CA-31063, Task no. 18211 and the University of California Energy Institute. Special thanks to UCSB divers, Shane Anderson, Dave Farrar, Dennis Divins, and underwater videographer, Eric Hessel. Views and conclusions in this document are those of the authors and should not be interpreted as necessarily representing the official policies, either expressed or implied of the U.S. government, or UCSB.

References

Allen, A.A., Schlueter, R.S., Mikolaj, P.G., 1970. Natural oil seepage at Coal Oil Point. Santa Barbara, California. Science 170, 974–977.

Blanchard, D.C., Syzdek, L.D., 1977. Production of air bubbles of a specified size. Chem. Eng. Sci. 32, 1109–1112.

Boles J.R., Eichhubl P., Garven G., Chen J., 2004. Evolution of a hydrocarbon migration pathway along a basin bounding fault: Evidence from fault cements. AAPG Bulletin 88, 947–970.

Boles, J.R., Clark, J.F., Leifer, I., Washburn, L., 2001. Temporal variation in natural methane seep rate due to tides. Coal Oil Point area, California. J. Geophys. Res. 106C11, 27077–27086.

Clark, J.F., Leifer, I., Washburn, L., Luyendyk, B.P., 2003. Compositional changes in natural gas bubble plumes: Observations from the Coal Oil Point Seep Field. Geo. Mar. Lett. 23, 187–193.

Clark, J.F., Washburn, L., Hornafius, J.S., Luyendyk, B.P., 2000. Dissolved hydrocarbon flux from natural marine seeps to the southern California Bight. J. Geophys. Res. 105, 11509–11522.

Clift, R., Grace, J.R., Weber, M.E., 1978. Bubbles, Drops, and Particles. Academic Press, London p. 380.

Duineveld, P.C., 1995. The rise velocity and shape of bubbles in pure water at high Reynolds number. J. Fluid Mech. 292, 325–332.

Etiope, G., Klusman, R.W., 2002. Geologic emissions of methane into the atmosphere. Chemosphere 49, 779–791.

Fischer P.J., 1978. Natural gas and oil seeps, Santa Barbara Basin, California. In California Offshore Gas, Oil, and Tar Seeps, (pp 1–62). State Lands Commission Report.

Fischer, P.J., Stevenson, A.J., 1973. In: Fischer, P.J. (Ed.), Natural hydrocarbon seeps, Santa Barbara basin, California, Santa Barbara Channel area revisited Field Trip Guidebook, Vol. 3. American Association of Petroleum Geology, Tulsa, OK, pp. 17–28.

Hornafius, J.S., Quigley, D., Luyendyk, B.P., 1999. The world's most spectacular marine hydrocarbon seeps (Coal Oil Point, Santa Barbara Channel, California): Quantification of emissions. J. Geophys. Res. 104, 20703–20711.

Johnson, B., Boudreau, B.P., Gardiner, B., Maass, R., 2002. Mechanical response of sediments to bubble growth. Mar. Geol. 187, 347–363.

Kennett, J.P., Cannariato, K.G., Hendy, I.L., Behl, R.J., 2003. Methane hydrates in Quaternary climate change: The clathrate gun hypothesis, vol. 54. AGU Washington p. 216.

Khalil, M.A.K., Rasmussen, R.A., 1995. The changing composition of the Earth's atmosphere. In: Singh, H.B. (Ed.), Composition, Chemistry, and Climate of the Atmosphere. Van Nostrand Reinhold, New York, pp. 50–87.

Kvenvolden, K.A., Reeburgh, W.S., Lorenson, T.D., 2001. Naturally occurring methane seepage—Workshop report. EOS 82, 457.

La Montagne M.G., Leifer I., Bergmann S., Vandewerfhorst L.C., Holden P.A, 2004. Bacterial diversity in marine hydrocarbon seep sediment. Environ. Microbiol. 6, 799–808.

Leifer, I., Patro, R., 2002. The bubble mechanism for transport of methane from the shallow sea bed to the surface: A review and sensitivity study. Cont. Shelf Res. 22, 2409–2428.

Leifer, I., MacDonald, I., 2003. Dynamics of the gas flux from shallow gas hydrate deposits: Interaction between oily hydrate bubbles and the oceanic environment. Earth Plan. Sci. Lett. 210, 411–424.

Leifer I., Boles J, 2005. Turbine seep-tent measurements of marine hydrocarbon seep forcing on second time scales. J. Geophys. Res.110, doi: 10.1029/2003JC002207.

Leifer, I., Clark, J., Chen, R., 2000a. Modifications of the local environment by a natural marine hydrocarbon seep. Geophys. Res. Lett. 27, 3711–3714.

Leifer, I., Patro, R., Bowyer, P., 2000b. A study on the temperature variation of rise velocity for large clean bubbles. J. Atm. Ocean Tech. 17, 1392–1402.

Leifer, I., Boles, J., Clark, J., Holden, P., LaMontagne, M., Luyendyk, B.P., Olman, C., Washburn, L., 2002. Predicting the fate of oil in the marine environment from the seabed to surface oil slicks and beyond. California and the World Oceans'02, Santa Barbara, CA 2002.

Leifer, I., Clark, J.F., Luyendyk, B., Valentine, D., 2003a. Subsurface hydrocarbon migration and its impacts. EOS 22, 364–371.

Leifer, I., De Leeuw, G., Cohen, L.H., 2003b. Optical measurement of bubbles: System, design and application. J. Atm. Ocean Tech. 20, 1317–1332.

Leifer, I., De Leeuw, G., Cohen, L.H., Kunz, G., 2003c. Calibrating optical bubble size by the displaced mass method. Chem. Eng. Sci. 58, 5211–5216.

Leifer I., Boles J., Clark J.F., Luyendyk B.P., 2004. The dynamic nature of marine hydrocarbon seepage. Environ. Geol. 46, 1038–1052.

MacDonald, I.R., Leifer, I., Sassen, R., Stine, P., Mitchell, R., Guinasso Jr., N.L., 2002. Transfer of hydrocarbons from natural seeps to the water column and atmosphere. Geofluids 2, 95–107.

MacDonald, I.R., Buthman, D.B., Sager, W.W., Peccini, M.B., Guinasso Jr., N.L., 2000. Pulsed flow of oil from a mud volcano. Geology 28, 10907–10910.

McDougal, T.J., 1978. Bubble plumes in stratified environments. J. Fluid Mech. 4, 655–672.

Mandelbrot, B.B., 2002. Gaussian self-affinity and fractals: Globality, the earth, 1/f noise and R/S. Springer, New York p. 654.

Marmur, A., Rubin, E., 1976. A theoretical model for bubble formation at an orifice submerged in an inviscid liquid. Chem. Eng. Sci. 31, 453–463.

Patro, R., Leifer, I., Bowyer, P., 2002. Better bubble process modeling: Improved bubble hydrodynamics parameterisation. In: Donelan, M., Drennan, W., Salzman, E.S., Wanninkhof, R. (Eds.), Gas Transfer and Water Surfaces AGU Monograph Volume 127, pp. 315–320.

Prather, M., Derwent, R., Ehhalt, D., Fraser, P., Sanhueza, E., Zhou, X., 1995. Other trace gases and atmospheric chemistry. In: Climate change 1994: Radiative forcing of climate change and an evaluation of the IPCC IS92 emission scenarios. In: Houghton, J.T., Meira-Filho, L.G., Bruce, J., Lee, H., Callander, B.A., Haites, E., Harris, N. (Eds.),. Cambridge University Press, Maskell, Cambridge United Kingdom, pp. 73–126.

Quigley, D.C., Hornafius, J.S., Luyendyk, B.P., Francis, R.D., Clark, J., Washburn, L., 1999. Decrease in natural marine hydrocarbon seepage near Coal Oil Point. California, associated with offshore oil production. Geology 27, 1047–1050.

Roy, L.A., Steinert, S., Bay, S.M., Greensteain, D., Sapozhnikova, Y., Bawardi, O., Leifer, I., Schlenk, D., 2003. Biochemical effects of petroleum exposure in hornyhead turbot (*Pleuronichthys verticalis*) exposed to a gradient of sediments collected from a natural petroleum seep in CA, USA. Aquatic Toxicol. 65, 159–169.

Sadhal, S., Johnson, R.E., 1983. Stoke's flow past bubbles and drops partially coated with thin films. J. Fluid Mech. 126, 237–250.

Tryon, M.D., Brown, K.M., Torres, M.E., Trehu, A.M., McManus, J., Collier, R.W., 1999. Measurements of transience and downward fluid flow near episodic methane gas vents. Hydrate Ridge, Cascadia. Geology 27, 1075–1078.

Tsuge, H., Hibino, S., Nojima, U., 1981. Volume of a bubble formed at a single submerged orifice in a flowing liquid. Internat. Chem. Eng. 21, 630–636.

Vagle, S., Farmer, D.M., 1998. A comparison of four methods for bubble size and void fraction measurements. IEEE J. Oceanic Eng. 23, 211–222.

Washburn, L., Clark, J.F., Kyriakidis P. The spatial scales, distribution, and intensity of natural marine hydrocarbon seeps near Coal Oil Point, California. Mar. Petrol. Geol., this issue, doi: 10.1016/j.marpetgeo.2004.08.006.

Washburn, L., Johnson, L., Gotschalk, C.G., Egland, E.T., 2001. A gas-capture buoy for measuring bubbling gas flux in oceans and lakes. J. Atm. Ocean Tech. 18, 1411–1420.